RESEARCH ARTICLE

# Experiments on turbulence beneath a free surface in a stationary field generated by a Crump weir: free-surface characteristics and the relevant scales

**Sandro Longo**

**Abstract** This work concerns the analysis of experimental instantaneous fluid levels and three-component fluid velocity measurements in a stationary flow field generated by a Crump weir in a laboratory flume using an ultrasonic distance sensor and a three-probe arrangement of an ultrasonic Doppler velocity profiler. The tests are characterised by different and increasing Froude numbers ($Fr = 0.10$–$0.38$), with the free surface of the fluid ranging from flat (low Froude number) to almost aerated (high Froude number). The statistics of the free surface are computed, and the relevant length and velocity scales are measured. A free-surface boundary layer was detected having a thickness proportional to the root mean square of the free-surface height series and with a velocity scale that related well to the free-surface elevation time gradient. The mean velocity profiles are presented. There are many indicators that a specific regime occurs with an optimal tuning between free surface and turbulence. In this regime, the length scales are raised.

**List of symbols**

| | |
|---|---|
| $\langle \dots \rangle$ | Space average operator |
| $\overline{\dots}$ | Time average operator |
| $\widetilde{\dots}$ | Phasic average operator |
| $\delta_v$ | Thickness of the viscous sub-layer |
| $\Phi_j$ | Volume fraction or concentration for the $j$ phase |
| $\Lambda_{zz}$ | Integral length scale in the vertical computed on using the vertical fluctuation velocity |

| | |
|---|---|
| $\rho$ | Mass density |
| $\sigma$ | Surface tension |
| $v$ | Kinematic fluid viscosity |
| $\zeta_0$ | Abscissa in the beam axis reference system |
| $\Theta$ | Temperature |
| $a$ | Weighting function |
| $\mathbf{A}, \mathbf{B}$ | Matrix for reference transformation |
| $a\_um_{rms}, a\_dm_{rms}$ | Root mean square of the up-midlevel amplitude (crests) and of the down-midlevel amplitude (troughs) |
| $c$ | Celerity of propagation of ultrasound |
| $d'$ | Head over the weir crest |
| $d$ | Water depth upstream |
| DNS | Direct numerical simulation |
| $f_{co}$ | Cut-off frequency |
| $f_e$ | Frequency of the carrier |
| $Fr_s$ | Froude number based on free-surface scales |
| $Fr_{upstream}, Fr$ | Froude number in the upstream section, in the section of measurement |
| FS | Full scale |
| $H, H_{rms}$ | Wave height, root mean square wave height |
| $H_{1/3}, H_{1/10}, \dots$ | Mean value of the first third, of the first tenth, … |
| $h, h_{meas}, h_{wave}$ | Instantaneous filtered value, measured value, value due to potential flow |
| $k$ | Coefficient |
| $L_0$ | Distance of the target |
| PDF | Probability density function |
| PIV | Particle image velocimetry |
| $Q$ | Volume discharge |
| Re, Re_s | Reynolds number, based on surface scales |

S. Longo (✉)
Department of Civil Engineering, University of Parma,
Viale G.P. Usberti, 181/A, 43100 Parma, Italy
e-mail: sandro.longo@unipr.it

| $R^2$ | Coefficient of determination |
|---|---|
| S/N | Signal to noise ratio |
| $t$ | Time |
| $T$ | Period of the waves, period of time average |
| $T_{mean}, T_{1/3}, \ldots$ | Period of the waves, mean value, mean value of the first third, … |
| $t_{prf}$ | Time between two subsequent pulses |
| US | Ultrasound |
| UVP | Ultrasonic Doppler velocity profiler |
| $u, v, w$ | Streamwise, spanwise, vertical fluid velocity |
| $u', v', w'$ | Streamwise, spanwise, vertical fluctuating fluid velocity |
| $u'_{rms}, v'_{rms}, w'_{rms}$ | Streamwise, spanwise, vertical root mean square value of the fluctuating fluid velocity |
| $u_i$ | Velocity component along the $i$ beam axis |
| $u_s$ | Velocity scale |
| $u_{upstream}, u_{ms}$ | Mean fluid velocity in the upstream section, in the section of measurement |
| $V$ | Volume of integration |
| $V_s$ | Velocity of the surface |
| $We_s$ | Weber number, based on surface scales |
| $x, y, z, x_i$ | Spatial co-ordinates |
| $\mathbf{x}, \mathbf{s}$ | Space vector |
| $X_j$ | Phasic function for the $j$ phase |
| $z_s$ | Instantaneous level of the free surface |

# 1 Introduction

An understanding of the structure and dynamics of free-surface turbulence is essential for the correct interpretation of many interface phenomena, and the need for measuring the characteristics of turbulence beneath a free surface arises from its role in many important phenomena that take place at interfaces. These include gas and heat exchange in the ocean, which have huge influences on the balance of chemicals and energy. In many engineering and industrial problems, most exchange takes place at the interface between a gas and a fluid, and many large-scale physical problems are governed by the characteristics of turbulence beneath an interface.

The free surface represents a boundary for the flow domain and imposes some conditions: the material derivative of the free surface must be zero, while the tangential stresses should be zero (unless a shear is exerted by the overflowing gas). The interaction between turbulence and a free surface is expected to vary with the level of turbulence. The two main measures for describing the phenomenon are the Reynolds number and the Froude number, which generally increase together. At reduced Froude numbers, a free surface is essentially unaffected by the turbulence of the flow beneath it, is almost flat and imposes a reduction in only the normal velocity component. In this way, it can be described as a slip-free, rigid, flat surface. At higher Froude numbers, the free surface is not flat, and an energy exchange with the fluid flow ensues. Such an exchange is assumed to be initially very limited, but it becomes quite strong when a free surface loses its connectivity and contains air bubbles and drops. A great variety of free-surface patterns and energy transfer mechanisms exist at a free surface, including capillary and gravity waves. A general description of the various levels of interaction between free surfaces and turbulence is reported in Brocchini and Peregrine (2001a). The authors describe the wide range of free-surface deformations that occur when there is turbulence at the surface, and they give specific attention to turbulence in the liquid medium. Their discussion considers the effects of gravity and surface tension on the action of kinetic turbulent energy, and the authors heuristically outline a two-parameter description of surface behaviour in terms of length scale and turbulent kinetic energy.

Several experimental results are reported in the literature, often obtained using sophisticated techniques that are necessary to describe the complexity of the flow field. Komori et al. (1989) used laser Doppler anemometry to measure fluid velocity, an infrared scanner to measure free-surface temperature and a cold film probe to measure the temperature in the flow field. Most of the techniques adopted are image based. An important experimental approach is the use of shadography (Settles 2001), which generates images that result from the refraction of light. Additionally, particle image velocimetry (PIV) has been used to evaluate the interaction between a free surface and the flow beneath (Weingand 1996). Laser scanning, with an output signal that is dependent upon the surface gradient, when used in conjunction with a laser Doppler anemometer and a PIV, seems to be useful for detecting the space-time characteristics of the flow (Savelsberg et al. 2006). Dabiri and Gharib (2001) combined digital image particle velocimetry and a reflective mode of the free-surface gradient detector method to evaluate the correlations between near-surface deformation and near-surface velocity and vorticity. Their device was able to measure elevation in the range of ±1.2 mm. Quiao and Duncan (2001) used PIV to study gentle spilling breakers and to detail the flow field in the pre-breaking and breaking conditions. Savelsberg et al. (2006) measured the gradient field along the line of a turbulent free surface using a laser scanning technique

coupled with laser Doppler anemometry and PIV. In this way, they were able to measure 2D velocity fields beneath the free surface. In the field, radar instruments in ships, satellites, buoys or pressure sensors give information on the free-surface elevation, but this information yields limited information about the mean flow field and turbulence.

More detailed information is obtained using direct numerical simulations (DNS), which are useful for the examination of low Froude number, free-surface turbulence (Shen et al. 1999). This method also allows for the evaluation of pressure correlations, although this is beyond present experimental capabilities. In these simulations, the free surface is essentially flat, and no interactions are detected except by their effects on the turbulence of a boundary layer (a region adjacent to the free surface). The authors also distinguish a viscous surface layer from a blockage layer: in the viscous surface layer, which has a thickness scaling with the square root of the local Reynolds number, large Reynolds numbers yield fast changes in the vorticity from the external value to its value at the free surface. In particular, at low Froude numbers, the vorticity at the free surface has only a vertical component. In the blockage layer, there is a redistribution of the turbulent intensity, with a reduction in vertical velocity fluctuations and an increase in horizontal velocity fluctuations. The blockage layer is thick on the macro-scale. This is not the only definition of the surface layer. Brocchini and Peregrine (2001b) describe the surface layer as the region occupied by two different phases, air and water; this definition can be used only if the free surface is disconnected, having either bubbles in water or droplets in air.

Some other sophisticated models of large-eddy simulation also show new and characteristic behaviours of turbulence flux near the interface (Shen and Yue 2001). Hong and Walker (2000) developed a set of Reynolds-averaged governing equations for turbulent free-surface flow, with additional terms respect to standard Reynolds-averaged equations representing the effects of the boundary conditions. They also detail on the origin of the surface current, as observed in many fluid flows interacting with the free surface, analysing the different role of Reynolds stress anisotropy and free-surface fluctuations.

In most (if not all) experiments and analyses, attention is focused on weak turbulence, with consequent weak and almost undetectable free-surface fluctuations. This is indicated by the fact that papers on this topic do not describe the statistics of the free surface. Here, we represent the flow field by a roller generated on a steady current by a Crump weir. The turbulence in the liquid is strong enough to interact with the free surface; surface tension is dominant and gravity is less important. The mean flow and turbulence patterns are typical of this specific flow field and dependent on the section being measured. Nevertheless, the results can be used to improve our knowledge of turbulence and free-surface interactions. To categorise the flow set-up, we refer to the framework introduced by Brocchini and Peregrine (2001a). Although some uncertainties arise in regard to the correct length scale, we find that some of the present tests are in the "wavy" domain, generally not breaking and without air inclusion, whereas the less energetic tests are in the "rippled" domain.

The phenomenon taking place downstream the crump weir is a classical hydraulic jump, essentially a non-breaking or undular in most tests. It is often used as a flow pattern to check models' assumptions, and several references can be found on the topic (Reinauer and Hager 1995; Khader and Elango 1974; Chanson and Brattberg 2000).

The velocity and level of the fluid were measured using ultrasound. This technique is not new, but its application and recent evolution provide a new method to study velocity measurements in complex flows. The technique was initially applied to measure the velocity at a single point, whereas 3D measurements were made possible using acoustic Doppler velocimetry (Kraus et al. 1994). It has been widely applied for measurements, in both the laboratory and the field (Shen and Lemmin 1997; Lemmin and Rolland 1997; Gordon and Oltman 2000; Hurther 2001; Hurther and Lemmin 2001; Miles et al. 2002). Ultrasonic measurements of the velocity fields beneath shoaling and breaking waves in the laboratory were obtained by Doering and Donelan (1997). They used a servo-hydraulic surface-following device to move an acoustic current metre and performed quasi-lagrangian measurements referring to the free surface.

Recently, ultrasonic Doppler velocimetry has taken advantage of new probe configurations and algorithms to elaborate the echo, and these allow fluid velocity measurements to be taken at several points (gates) along the ultrasound (US) beam axis, thereby obtaining the velocity profile. The technique was initially applied for medical purposes, such as measuring flow in blood vessels and the heart. It can be used in optically opaque fluids, such as mud, and in high-temperature fluids, such as liquid sodium (Eckert and Gerbeth 2002). Ultrasonic Doppler velocity profiler (UVP) can give information on spatio-temporal velocity with a data rate that is virtually independent of the seeding concentration [see Takeda (1999a) for a description of US techniques] and is well suited for giving information in a complex flow field, especially if the spatial distribution is of major interest (e.g., Takeda 1999b). Longo et al. (2001) measured fluid velocity in breaking waves and in the subsequent bore in laboratory experiments with regular waves. The effects of air or gas bubbles in the flow field were also described in detail, with the specific aim of validating data from measurements taken in aerated bores and breaking waves (Longo 2006). Kantoush

et al. (2008) used UVP in a configuration that was similar to that described here and found good agreement between large-scale particle image velocimetry, UVP and numerical simulation methods. Amini (2009) investigated the velocity profiles and the instability at the interface of a two-phase water–oil fluid. De Cesare and Boillat (2006) also provide an extensive description of the application of US Doppler methods in hydraulic modelling.

This paper is organised as follows: The experimental procedures and set-up, including the main features of the measurement devices, the data acquisition and the uncertainty analysis, are described in Sect. 2. Section 3 is devoted to describing and discussing the results, with specific attention given to the free-surface fluctuation statistics and the mean velocity. The conclusions are outlined in the final section.

## 2 Experimental apparatus and procedures

### 2.1 Description of the device and uncertainty analysis of the instruments

The present analysis refers to experiments in a flume, with free-surface turbulence generated by a Crump weir. The experimental set-up is shown in Fig. 1. The flume was 15 m long, 0.30 m wide and 0.47 m high, and it was supplied by a pump feeding a small tank at one end. The inflow had a flow conditioner to remove swirl and was constructed with several small circular cylinder tubes parallel to the flume axis. The flow rate was monitored using a magnetic flow metre that was accurate to within 0.5% of the instantaneous value. The Crump weir was made with PMMA and was symmetric, with upstream and downstream slopes of 1:2 and a crest height of 17 cm with respect to the bottom of the flume. The crest was 7.1 m from the tank, and the approaching flow had a flat surface with limited turbulence. The measurement section was 0.9 m past the weir (where the mean level was maintained at $\sim 150$ mm) and was controlled by a bottom-hinged flap gate in the exit section of the flume. In all tests, we obtained a modular flow condition, with the head over the weir crest varying from $\sim 20$ mm (the minimum discharge in the tests) to $\sim 90$ mm (the maximum discharge in the tests). The approaching flow had Froude numbers that lay in the range 0.02–0.14, and a supercritical flow developed on the downstream face of the weir. The flow turned to a subcritical flow (Fr = 0.10–0.38) after a weak jump that was located well upstream of the measuring section. The main parameters of the inflow are reported in Table 1. Pictures showing the free-surface details for two different tests are shown in Fig. 2.
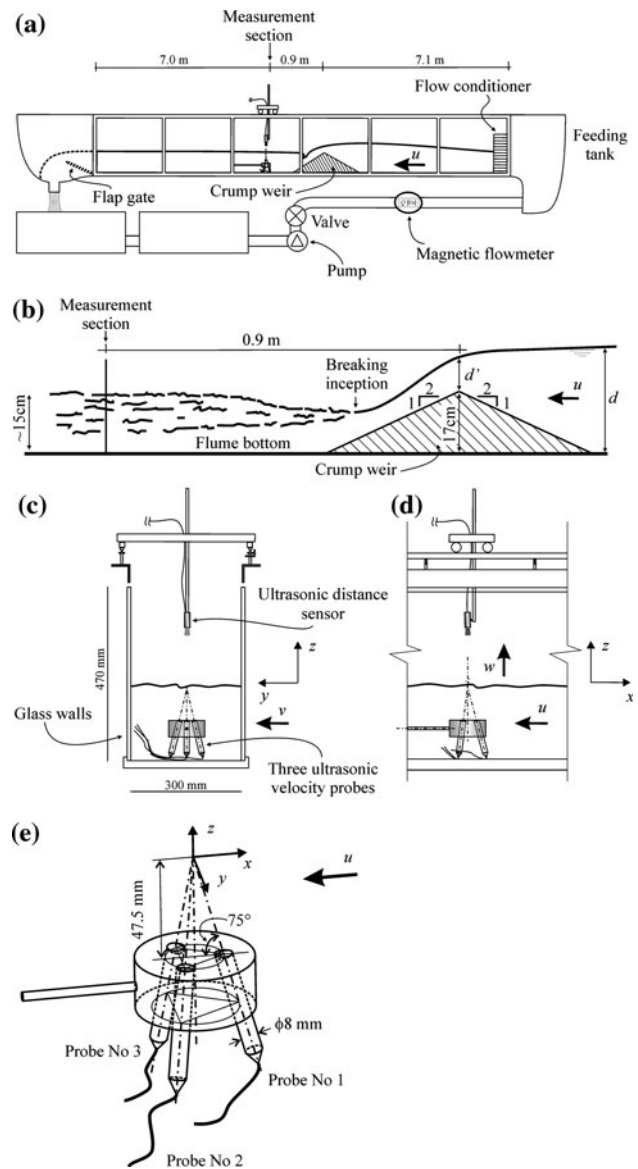


**Fig. 1** Sketch of the probes and reference system. **a** Schematic of the set-up and **b** details of the Crump weir. **c** Cross section and **d** lateral view of the experimental flume. **e** The probes

In the present study, the air–water interface will be referred to as the free surface. Free-surface elevations were measured using an ultrasonic sensor (Turck Banner Q45UR, 2002) based on flight-time having a carrier at 10 MHz, with temperature compensation and a sensing range of 50–250 mm (the distance of the target from the emitter/receiver). The response time was 10 ms.

Uncertainties in the ultrasonic distance measurements arose due to strong spatial gradients of the free surface that generated lost echoes and to gradients of temperature along the path of the sound that modified the celerity. In addition, the measurements were not precisely local, as the ultrasonic beam diverged with a 3.5° angle, and the area of

**Table 1** Flow conditions for the experiments

| Test (#) | $Q$ (l/s) | $d'$ (mm) $\pm$ 0.1 mm | $d$ (mm) $\pm$ 0.1 mm | $u_{upstream}$ (m/s) $\pm$ 1% | $Fr_{upstream}$ (.) $\pm$ 1% | $u_{ms}$ (m/s) | Fr (.) |
|---|---|---|---|---|---|---|---|
| 66 | 17.3 $\pm$ 0.2 | 64.0 | 260.7 | 0.221 | 0.139 | 0.39 $\pm$ 0.03 | 0.32 $\pm$ 0.04 |
| 65 | 15.2 $\pm$ 0.2 | 59.6 | 253.2 | 0.200 | 0.127 | 0.33 $\pm$ 0.03 | 0.28 $\pm$ 0.03 |
| 61 | 10.1 $\pm$ 0.1 | 45.0 | 233.1 | 0.143 | 0.0952 | 0.22 $\pm$ 0.01 | 0.18 $\pm$ 0.01 |
| 62 | 6.64 $\pm$ 0.07 | 34.1 | 218.6 | 0.102 | 0.0695 | 0.146 $\pm$ 0.003 | 0.121 $\pm$ 0.005 |
| 63 | 3.69 $\pm$ 0.03 | 22.9 | 202.9 | 0.0630 | 0.0432 | 0.082 $\pm$ 0.001 | 0.068 $\pm$ 0.001 |
| 64 | 1.87 $\pm$ 0.01 | 14.9 | 191.8 | 0.0330 | 0.0239 | 0.041 $\pm$ 0.001 | 0.033 $\pm$ 0.001 |

$Q$ is the water discharge, $d'$ is the head over the weir, $d$ is the water depth upstream, $u_{upstream}$ and $u_{ms}$ are the mean velocity as evaluated upstream and in the section of measurement, $Fr_{upstream}$ and $Fr$ are the Froude number upstream and in the section of measurement
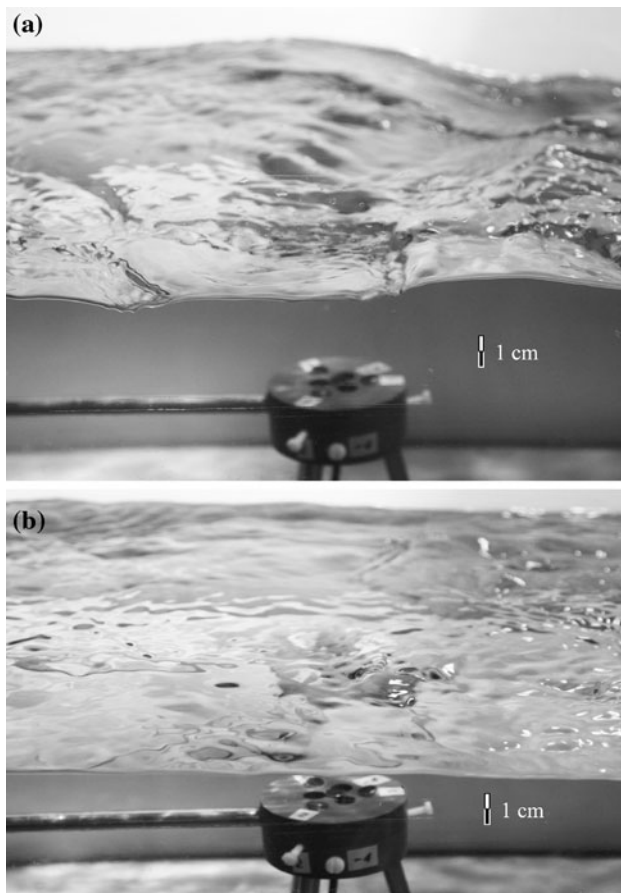


**Fig. 2** Free-surface details during test no. 66 **a** and test no. 61 **b**

averaging was 10-mm-diameter circle at the distance of the measurements.

The first source of uncertainty was overcome by holding the last measured value in case of an absence of echo, with a negligible loss of information. The uncertainty due to temperature gradients along the path of the sound could be quantified. Assuming a linear variation of the temperature between the emitter and the target, the relative uncertainty is equal to:

$$\frac{\Delta L}{L_0} = \frac{\Theta_1 - \Theta_0}{4\Theta_0} \tag{1}$$

$\Theta_0$ is the temperature near the emitter/receiver, $L_0$ is the distance to the target and $\Theta_1$ is the temperature near the target. We have assumed a negligible uncertainty in the time of flight measurements. Assuming $\Theta_0 = 293$ K and $\Theta_1 = \Theta_0 \pm 1$ K, the maximum uncertainty is equal to $\pm 0.2$ mm.

The final factor is the non-stationary nature of the target. Considering that the echo is generated by a moving surface, a Doppler shift is expected equal to $(2V_s/c)f_e$, where $V_s$ is the velocity of the surface, $c$ is the celerity of US propagation in air and $f_e$ is the frequency of the carrier. Fortunately, US waves are not dispersive in air, and the small frequency shift does not affect the computation of the distance of the target (here, the instantaneous water level measurement).

Under our experimental conditions, the overall uncertainty in the free-surface level measurements (including the non-linearity and repeatability of the instrument) was estimated to be $\pm 0.3$ mm.

Measurements of the fluid velocity below the free surface were taken using an array of three probes connected to an UVP (Signal Processing, Switzerland, model DOP2000, 2005), and the carrier frequency of the probes was 8 MHz (TR0805LS) (the arrangement of the probes is shown in Fig. 1e). The transducers had active element diameters of 5 mm in an 8-mm (diameter) cylindrical plastic housing. The arrangement of the three probes was chosen to guarantee an overlap of the measurement volume in the area of interest just below the mean free surface, with the aim of mapping out the near-surface flow field. To increase the S/N ratio, the water was seeded with clay, and this proved to be an excellent seeding material.

Each transducer measured the axial velocity component as a function of the axial position. The velocity profile was measured in several tens of spatial positions (gates), starting from 3 mm in front of the probe head and was assumed to be in the centre of the measuring volumes. The

measuring volume of a single gate was approximately disc shaped, with a thickness related to the operating condition and a diameter that was almost invariant (nominally equal to 5 mm in the near-field zone, $\sim$33 mm long for the probe used in water). The measuring volume increased in the far field progressively due to lateral spreading of the US energy, with a half diverging angle of 1.2° for the probe used in water. The actual diameter of the measuring volume is smaller than the nominal volume if the correct sensitivity level and beam power are selected. In fact, a reduced sensitivity during the echo reception (i.e., a high level of energy of the echoes requested to process the signal) and a high power of the US beam favour the back-scatter of the particles near the axis of the beam (the US power decreases in the radial direction as well as the axial direction) and thus focus the volume of measurements in the near-axis region. Balancing this, multiple particles or micro-eddies present in the volume of measurement scatter the echoes and broaden the spectral peak, whereas diffraction tends to enlarge the measurement volume. The thickness of the sampling volumes is assumed to be equal to half the wavelengths contained in a burst, unless the electronic bandwidth of the instrument is limiting. In our experimental set-up, this last variable is the limiting factor that determines the minimum thickness of the sampling volume (0.68 mm in water). The overall size of the measurement volumes allows only the detection and analysis of macro-turbulence, but this limitation is outweighed by some advantages, such as the large number of measurement points that are almost simultaneously available. In addition, the larger size of the measurement volumes is in the horizontal plane, and, in the flow field of the present experiments, the fluid velocity has a moderate spatial gradient in the horizontal direction. The most important spatial gradient is expected in the vertical dimension, and the resolution in the vertical axis is comparable to the resolution obtained using laser Doppler anemometry, PIV or thermal anemometry. The distance between two gates varied in different tests from 0.72 to 0.95 mm, as measured along the beam axis using non-overlapping measurement volumes. The space step between two adjacent gates was reduced by cos(15°) in the vertical direction and varied from 0.70 to 0.92 mm. Each profile was obtained as an average of eight emissions of a four-wave burst. The acquisition was multiplexed with circular scanning of a single profile for each probe. The time lag between two different probe measurements was $\sim$0.03 s on average, whereas the time lag of the pulse from one gate to another was $k\delta z/c$, where $k$ is a coefficient ($\sim$2), $\delta z$ is the distance between two gates and $c$ is the US celerity in water. The velocity resolution was 1/128 (1 least significant bit) of the velocity range ($\sim$0.8% FS). For all tests, this was better than 4 mm/s (the velocity measured along the probe axis).

There are some effects to be considered in evaluating the reliability of the measurements made using UVP. The presence of the moving interface generates a Doppler shift that is highly energetic and can persist in the flow field as a stationary signal. The elimination of these stationary components by high-pass filtering implies an increase in the dynamic of the analysed echoes and a reduction in the sensitivity of low velocity measurements. Unfortunately, the Doppler frequency shift induced by these mobile interfaces cannot be removed if its value is the same as that of the flowing particles. To balance all these effects, the presence of some artefacts is tolerated.

The main sources of uncertainty for the UVP are Doppler noise, the presence of air bubbles or highly reflective interfaces and the gradient of temperature in the liquid medium.

Doppler noise is essentially a Gaussian white noise and depends on the seeding particles and on the presence of gas bubbles. The effects of gas bubbles are quite dramatic: even though the celerity of the US carrier is essentially not affected if the bubble void fraction is <0.1, the UVP system measures the bubbles' velocities, and these can be much different from the fluid velocity if the bubbles are large (Longo 2006). In the presence of bubbles or highly reflective interfaces, several velocity spikes are recorded that are not due to turbulence. For this reason, we limited the experiments to non-aerated flows.

The uncertainty in the position of the gates and in the fluid velocity evaluation is due to the mean celerity of the ultrasounds, which is affected by the temperature and density of the fluid. Considering pure water and assuming that the temperature varies linearly between the emitter and the gate, the relative uncertainty in the position of the gate is equal to:

$$\frac{\Delta L}{L_0} = \frac{c_1^2 - c_0^2}{4c_0^2}. \tag{2}$$

Here, $L_0$ is the distance of the gate from the emitter/receiver as measured at the nominal uniform celerity $c_0$ (the celerity near the emitter/receiver with a fluid temperature $\Theta_0$) and $c_1$ is the celerity near the gate with a local fluid temperature equal to $\Theta_1$. The uncertainty in travel time measurements has been neglected because the electronics allow for very accurate estimations of the interval time. Assuming $\Theta_0 = 288$ K and $\Theta_1 = \Theta_0 \pm 1$ K, then $c_0 = 1462.8$ m/s, $c_1 = 1462.8 \pm 2.7$ m/s, the relative uncertainty $\Delta L/L_0 = 0.1\%$ and the absolute uncertainty $= \pm 0.1$ mm at a distance of 100 mm.

The evaluation of the uncertainty in fluid velocity evaluation requires a short description of the principle of the UVP that we used. In the UVP adopted, the emitter periodically sends a short ultrasonic burst (four waves per burst in the set-up used), and a receiver (coincident with

the emitter) collects echo issues from targets that may be present in the path of the ultrasonic beam. By sampling the incoming echoes at the same time relative to the emission of the bursts, the displacements of scatters along the beam axis are detected, and from these, the fluid velocity along the beam axis (assumed equal to the velocity of the scatters) is computed as:

$$u = \frac{c(t_2 - t_1)}{2t_{prf}}, \tag{3}$$

where $t_{prf}$ is the time between two subsequent pulses, $t_1$ is the travel time of the first pulse and $t_2$ is the travel time of the second pulse. Assuming that the two events, "travel of the first pulse" and "travel of the second pulse", are not correlated, the absolute uncertainty in the velocity estimation can be computed as:

$$\Delta u = \frac{L_0}{2t_{prf}} \frac{\Delta(L_2 - L_1)}{L_0} = \frac{L_0}{t_{prf}} \frac{\Delta L}{L_0}. \tag{4}$$

This is very large for most of the operating conditions (e.g., setting $t_{prf} = 3 \times 10^{-4}$ s for measurements in a gate at $L_0 = 100$ mm and assuming $\Delta L/L_0 = 0.1\%$ results in $\Delta u = 0.33$ m/s). In practical situations, if turbulence in the flow field has a time scale larger than $t_{prf}$, the fluctuations of celerity along the path have a similar pattern for the two subsequent pulses and this results in $\Delta(L_2 - L_1) \ll 2\Delta L$. In addition, the velocity is estimated as the average of several bursts (eight in the present experimental set-up), with a consequent reduction in the uncertainty.

A last source of uncertainty arises from the finite size of the measurement volumes (Kikura et al. 2004), which affects the velocity measurements and the Reynolds stress estimates. Here, this uncertainty is negligible with respect to the other sources of uncertainty.

The overall accuracy in the velocity measurements under carefully controlled conditions can be assessed as 3% of the instantaneous value, with a minimum equal to 0.8% of the full scale (less than 4 mm/s for most tests).

## 2.2 Data acquisition and analysis

Free-surface elevation data was acquired at 100 Hz using a DAQ 12-bit board by National Instruments with a low-pass filter at 25 Hz. Velocity measurements were stored independently by a second dedicated PC triggered to free-surface elevation data by an external cable, in order to have data of fluid velocity and of free-surface elevation with a common time origin. The frequency of acquisition of the velocity depends on the UVP set-up and cannot be forced to a specific value. Free-surface data were sub-sampled at the lower rate for a proper timing of free-surface elevation (higher data rate) and velocity measurements (lower data rate). Then, velocity data were elaborated in order to obtain the mean values of fluid velocity and of the Reynolds tensor in an Eulerian frame with a coordinate system having its origin at the mean water level.

Free-surface elevation was also statistically analysed in the time domain with a zero-crossing analysis in order to extract the root mean square height ($H_{rms}$) and several zero(-up)-crossing statistical estimators, as the mean value of the one-third of the fluctuations height ($H_{1/3}$), of the one-tenth ($H_{1/10}$), of the one-twentieth ($H_{1/20}$). Also the mean period $T_{mean}$ was computed. In order to check the asymmetry of the free-surface shape (possibly crest different from trough), the root mean square values of the crest (up-midlevel amplitude $a\_um_{rms}$) and of the troughs (down-midlevel amplitude $a\_dm_{rms}$) have been evaluated. The results are summarised in Table 2.

Before computing some relevant state variables, we need to clarify the terminology and the average operators. In the Eulerian frame, the data were generally elaborated using the classical time-space average and the phasic average. Considering any tensor $\mathbf{Q}$ function of space $\mathbf{x}$ and time $t$, the time average is equal to

$$\overline{\mathbf{Q}(\mathbf{x})} = \frac{1}{T} \int_T \mathbf{Q}(\mathbf{x}, t) dt \tag{5}$$

and is coincident with the ensemble average if the ergodic hypothesis holds.

Considering a generic weighting function $a(\mathbf{s})$ (which can be uniform and equal to one), where $\mathbf{s}$ is a space vector describing the volume of integration $V$, the space average of $\mathbf{Q}$ is

$$\langle \mathbf{Q} \rangle = \int_V \mathbf{Q}(\mathbf{x} + \mathbf{s}, t) a(\mathbf{s}) dV \tag{6}$$

The phasic average operator extends only to the time interval during the presence of a phase and is obtained by introducing the phasic function $X_j(\mathbf{x}, t) = 1$ if the vector position $\mathbf{x}$ is in the phase $j$ at the time $t$; otherwise, $X_j(\mathbf{x}, t) = 0$. The phasic average operator is defined as

$$(\widetilde{\ldots}) = \frac{\int_V X_j(\mathbf{s}, t) \mathbf{Q}(\mathbf{x} + \mathbf{s}, t) a(\mathbf{s}) dV}{\int_V X_j(\mathbf{s}, t) dV} = \frac{\langle X_j(\ldots) \rangle}{\langle X_j \rangle}$$
$$= \frac{\langle X_j(\ldots) \rangle}{\Phi_j} \tag{7}$$

$\Phi_j$ is the volume fraction or concentration (sometimes called the intermittency factor) of the $j$ phase. In the present analysis, only the water phase is of interest and the suffix $j$ is omitted. Hereafter, the symbols of the different average operators are generally omitted and the kind of average is explicitly mentioned or is clear from the context. See also Misra et al. (2008) on using the intermittency function to characterise a two-phase flow region of a breaker.

**Table 2** Free-surface zero-crossing statistics

| Test (#) | $H_{rms}$ (mm) | $T_{mean}$ (s) | $H_{1/3}$ (mm) | $H_{1/10}$ (mm) | $H_{1/20}$ (mm) | $H_{max}$ (mm) | $a\_um_{rms}$ (mm) | $a\_dm_{rms}$ (mm) | $u_s$ (mm/s) | Waves (no.) |
|---|---|---|---|---|---|---|---|---|---|---|
| 66 | 12.09 | 0.29 | 17.34 | 22.17 | 24.13 | 28.49 | 7.00 | 6.14 | 130.8 | 438 |
| 65 | 10.96 | 0.33 | 15.62 | 19.89 | 22.02 | 32.82 | 6.24 | 5.63 | 103.3 | 1,023 |
| 61 | 5.25 | 0.34 | 7.68 | 9.92 | 11.15 | 14.15 | 5.30 | 4.95 | 52.8 | 503 |
| 62 | 2.44 | 0.26 | 3.57 | 4.78 | 5.31 | 7.26 | 2.92 | 2.80 | 37.7 | 1,015 |
| 63 | 1.21 | 0.32 | 1.66 | 2.26 | 2.62 | 4.13 | 1.36 | 1.41 | 20.8 | 870 |
| 64 | 0.77 | 0.66 | 0.95 | 1.19 | 1.38 | 2.76 | 0.54 | 0.83 | 8.61 | 402 |

In many situations, the presence of waves requires the separation of their contribution in the flow field. The problem of separating waves and eddies, essentially a potential and a rotational component of the flow field (even though vorticity is not always turbulent, but turbulence is always vortical), is still unsolved. In the case of progressive waves, the stream function method by Dean (1965) can be applied to permanent non-breaking shape waves. Thornton (1979) suggested the evaluation of the potential component as the part of the flow field coherent with the free-surface elevation. This evaluation is based on the assumption that the free surface is affected only by the waves and cannot be applied to the present experiments aiming at quantifying turbulence effects on the free surface. Nadaoka (1986) proposed a method based on the Fourier decomposition of the flow field, with the spectrum of the potential field computed using velocity data at a level where vorticity is absent. Unfortunately, the flow field of the present experiments is turbulent (and, as a consequence, vortical), and a reference velocity cannot be obtained. A last method is based on filtering the velocity data, assuming that below a frequency threshold, the velocity is due to waves and all the residual contribution is due to turbulence. The results usually vary with the threshold. In the present experiments, all the above-mentioned methods reveal their limitations, but considering the importance of detecting the different contribution due to waves (potential flow) and turbulence, we decided to use the filtering method. Much care is needed in assessing the absolute validity of the results.

To separate the potential flow and the turbulent components, the cut-off frequency of the velocity time series has been fixed by observing the power spectrum of the vertical velocity. It generally shows a knee at $\sim 3$ Hz, with an almost linear decay at higher frequencies. The position of the knee is based on subjective judgment and is slightly different at different levels. It is also expected to increase at increased turbulence levels, as the turbulence energy tends to move towards smaller length scales and, hence, higher frequencies. Due to a certain degree of arbitrariness in the choice of the cut-off frequency, we simply assumed $f_{co} = 3$ Hz for all tests at all levels. An example of the instantaneous and filtered vertical velocity time series is

shown in Fig. 3 for test no. 66 at the gate at level $z = -19.9$ mm. A good correlation is observed between the free-surface water level and the filtered velocity, even though we also need to observe possible correlations between the free surface and the turbulence.

The values are computed for further analysis as $h = h_{meas} - h_{wave}$, where $h_{meas}$ is the measured value and $h_{wave}$ is the low-pass-filtered value of $h_{meas}$, assumed to be representative of the contribution of the potential flow field.

The three probes measured the fluid velocity components along the three beam axes, $u_1$, $u_2$ and $u_3$ (see the reference system in Fig. 1e). The velocity components along the $x$, $y$ and $z$ axes ($u$ in the streamwise, $v$ in the spanwise and $w$ in the vertical directions) can be obtained by transforming the velocity:

$$\begin{Bmatrix} u \\ v \\ w \end{Bmatrix} = \mathbf{A} \cdot \begin{Bmatrix} u_1 \\ u_2 \\ u_3 \end{Bmatrix}. \tag{8}$$

$\mathbf{A}$ is the matrix of transformation.

The velocities $u_1$, $u_2$ and $u_3$ refer to the gates along the axes of the three probes at equal distances from the head of the probes (i.e., having equal abscissa in the axial reference
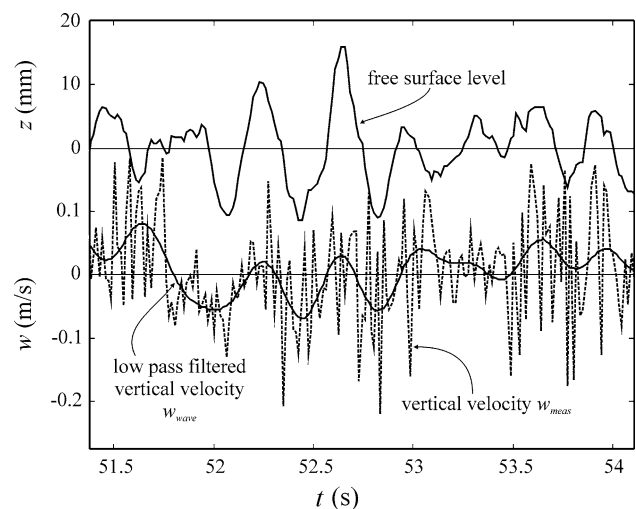


**Fig. 3** Vertical velocity: instantaneous and low-pass-filtered time series. Test no. 66, $H_{rms} = 12.09$ mm, gate at $z = -19.9$ mm

of each probe). Due to multiplexing acquisition, the velocities are acquired with a time lag $\Delta t$, equal to one-third of the scanning time:

$$u_1(\varsigma_0, t - \Delta t), u_2(\varsigma_0, t), u_3(\varsigma_0, t + \Delta t), \tag{9}$$

where $\varsigma_0$ is the abscissa in the axial reference. Developing in a Taylor series in the neighbourhood of $t$, the velocities reduced at time $t$ are

$$u_1(\varsigma_0, t) = u_1(\varsigma_0, t - \Delta t) + \frac{\partial u_1}{\partial t}\Big|_{\varsigma_0, t - \Delta t} \cdot \Delta t + O(\Delta t^2)$$
$$u_3(\varsigma_0, t) = u_3(\varsigma_0, t + \Delta t) - \frac{\partial u_3}{\partial t}\Big|_{\varsigma_0, t + \Delta t} \cdot \Delta t + O(\Delta t^2), \tag{10}$$

and the transformation corrected for the time lag reads

$$\begin{Bmatrix} u(z,t) \\ v(z,t) \\ w(z,t) \end{Bmatrix} = \mathbf{A} \cdot \begin{Bmatrix} u_1(\varsigma_0, t - \Delta t) \\ u_2(\varsigma_0, t) \\ u_3(\varsigma_0, t + \Delta t) \end{Bmatrix}$$
$$+ \mathbf{B} \cdot \frac{\partial}{\partial t} \begin{Bmatrix} u_1(\varsigma_0, t - \Delta t) \\ u_2(\varsigma_0, t) \\ u_3(\varsigma_0, t + \Delta t) \end{Bmatrix} \cdot \Delta t + O(\Delta t^2), \tag{11}$$

where

$$\mathbf{B} = \begin{bmatrix} A_{11} & 0 & -A_{13} \\ A_{21} & 0 & -A_{23} \\ A_{31} & 0 & -A_{31} \end{bmatrix}. \tag{12}$$

A total of 24,000 profiles (all probes) were recorded in each test for further analysis, with a data rate equal to $\sim 30$ profiles per second (three components of velocity were measured at each gate).

## 3 Results and discussion

### 3.1 Free-surface fluctuations

Six tests were performed with values of $H_{rms}$ ranging from less than $\sim 1$ to $\sim 12$ mm, as shown in Table 2, which also includes some other statistical estimators. The free-surface patterns in two tests are shown in Fig. 2. The zero(-up)-crossing analysis of the free surface reveals a small asymmetry of the free-surface fluctuations, and generally, the down-midlevel amplitude $a\_dm_{rms}$ is smaller than the up-midlevel amplitude $a\_um_{rms}$, except for low $H_{rms}$ values.

The typical probability density function (PDF) of the free-surface disturbance heights, as evaluated using the zero(-up)-crossing analysis, is shown in Fig. 4, (test no. 66, $H_{rms} = 12.09$ mm is presented). The height distribution (crest-trough distance in waves as detected on using a zero-up-crossing analysis) recalls a Rayleigh probability density function, which can be obtained by starting from a normal distribution of the free-surface disturbance levels.
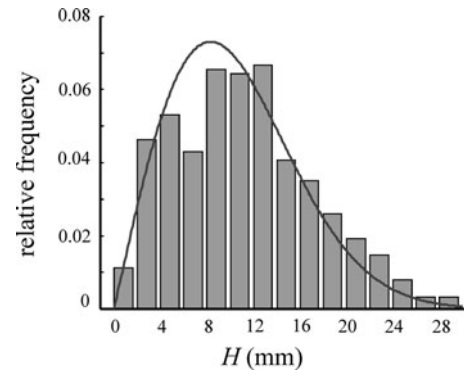


**Fig. 4** Probability density function of free-surface disturbance height elevations. Test no. 66. The fitted Rayleigh distribution is shown
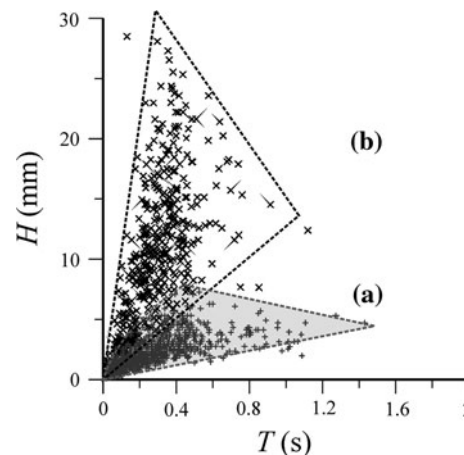


**Fig. 5** Height ($H$ from crest to through) versus time period ($T$) for two different tests **a** $H_{rms} = 2.44$ mm; **b** $H_{rms} = 12.09$ mm

The maximum period for a given fluctuation depends on the geometry of the system and can assume different values for different flow fields. The minimum period (maximum frequency) is limited by free-surface tension and micro-breaking, which induce a transfer of energy to higher periods. In the present experiments, micro-breaking occurs only for test no. 66. The plots in Fig. 5 show that the band of periods increases up to a maximum value of $H$ ($H$ is the wave height from crest to trough), then decreases with the highest fluctuations, which tend to have a characteristic period almost equal to 0.4 s. This selection process is shown more clearly in the plots in Fig. 6, which report the frequency domain analysis of the time series.
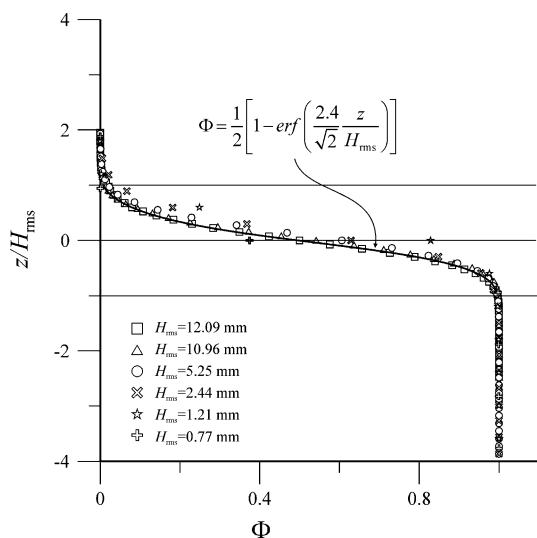
Most of the energy is stored at a frequency corresponding to the higher fluctuation period (0.4 s), even though a non-negligible amount of energy is stored at a larger period (2 s). The power spectrum of the free-surface elevation shows a main peak between $\sim 2.2$ and 2.6 Hz (see insert in Fig. 6). From a dynamic point of view, the system behaves as a non-linear oscillator vibrating at the
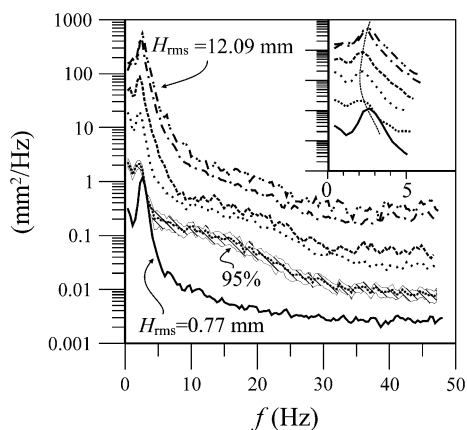
**Fig. 6** Power spectrum of free-surface elevation. For one test, the band at the 95% confidence level is also shown



**Fig. 7** Water concentration profiles
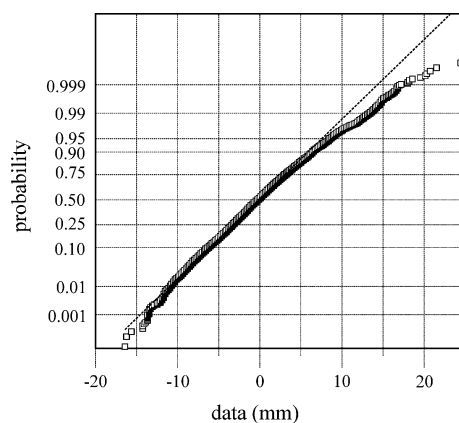


**Fig. 8** Normal probability plot of free-surface elevation for test no. 66. $H_{rms} = 12.09$ mm

$$\Phi = \frac{1}{2}\left[1 - \mathrm{erf}\left(\frac{a}{\sqrt{2}}\frac{z}{H_{rms}}\right)\right], \text{ for } -H_{rms} < z < H_{rms}. \quad (14)$$

The best fit is computed with $a = 2.4$. The fit has a very high coefficient of determination, $R^2 = 0.99$, even though the experimental data distribution is a distorted normal distribution, as confirmed by the probability plot in a Gaussian chart of the data (Fig. 8). Note that a normal distribution is assumed to be the distribution characteristic of the free-surface elevation in a turbulent splashing regime (Brocchini and Peregrine 2001b). This is not the case in the present tests, but the normal distribution is also generally characteristic of waves with a narrow-band spectrum (Goda 2000). The larger experimental persistence of water at low $\Phi$ can be attributed to the broadness effects of the spectrum.

### 3.2 Mean velocity

In the velocity measurements presented herein, the instantaneous (filtered) velocities $u$, $v$ and $w$ were elaborated to extract the time mean velocity and the phasic mean velocity. Mean (time or phasic) velocities are indicated as $\bar{u}$ (in the streamwise horizontal direction, negative $x$), $\bar{v}$ (in the spanwise horizontal direction, $y$) and $\bar{w}$ (in the vertical direction, $z$, positive upward). The fluctuating components are computed as $u' = u - \bar{u}$. The profiles for the two extreme tests are shown in Figs. 9 and 10. For an almost flat free surface ($H_{rms} = 0.77$ mm), the streamwise and spanwise velocity components are nearly zero at the free surface and increase linearly downward, with a maximum at $z = -4$ mm. For the test with the highest level of free-surface fluctuations ($H_{rms} = 12.09$ mm), the phasic average mean velocity profiles show an irregular behaviour in the free-surface boundary layer.

We have already mentioned several definitions of the free-surface boundary layer. A more general definition for

main peak frequency but with an added subharmonic component.

For many computations, the water concentration or volume fraction of the water (also called the intermittency factor) varies from zero (no water for the entire duration) to unity (water always present) and is an important variable.

The experimental water concentration profile (Fig. 7) shows an almost linear variation in the range $\pm H_{rms}$, with a very smooth damping in the range $[H_{rms}, 2H_{rms}]$. For most purposes, we can assume that

$$\Phi = \frac{1}{2}\left(1 - \frac{z}{H_{rms}}\right), \text{ for } -H_{rms} < z < H_{rms}. \quad (13)$$

However, a better fit can be obtained by assuming a normal distribution of the free-surface elevation, leading to the following expression:
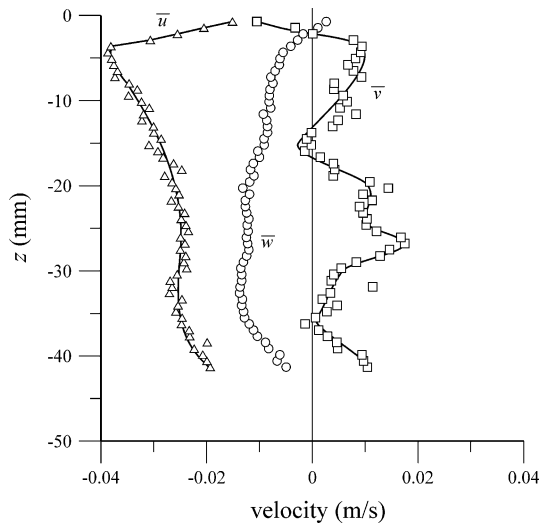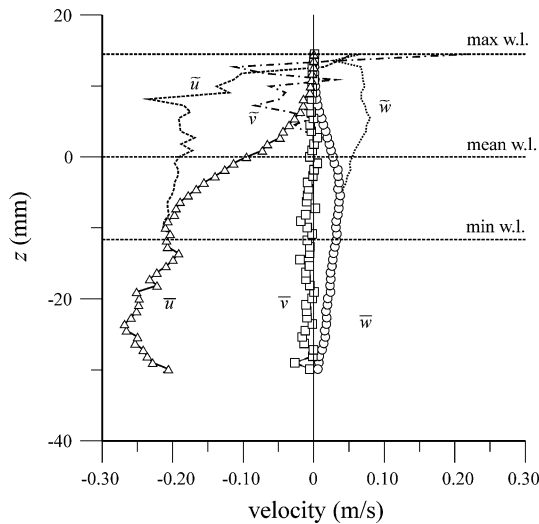
**Fig. 9** Test no. 64, $H_{rms} = 0.77$ mm. Mean velocity. Symbols refer to time average, lines refer to phasic average



**Fig. 10** Test no. 66, $H_{rms} = 12.09$ mm. Mean velocity. Symbols refer to time average, lines refer to phasic average

the free-surface boundary layer defines it as a part of the fluid domain controlled by the free-surface characteristics, with a scale related to the free surface. We will adopt this definition here.

This flow is different from that in an open channel, which usually shows a streamwise reduction in velocity near the free surface but the velocity becomes finite at the free surface. The measured mean velocity distribution is specific to the flow generated by the weir and is expected to vary at different downstream locations. In some locations, a counterflow mean velocity is also expected. Some spikes are occasionally present, especially for low mean velocities. As already described in §2, these spikes are due to

stationary echoes, but they are of similar magnitude to the overall accuracy of the flow velocity measurements.

The hypothesis that the free-surface dynamics and the turbulence near the free surface are strictly correlated suggests that $H_{rms}$ be chosen as the length scale and that $u_s = \sqrt{(dz_s/dt)^2}$ ($u_s$ is the root mean square value of the free-surface vertical velocity, where $z_s$ is the instantaneous vertical position of the free surface) be chosen as the velocity scale in the free-surface boundary layer. The material derivative is approximated by the partial derivative, i.e., $dz_s/dt \simeq \partial z_s/\partial t$.

Note that other length scales are suggested in the literature, such as the integral length scale based on autocorrelation of velocity fluctuations (Calmet and Magnaudet 2003), but as will be made clear in the following paragraphs, $H_{rms}$ appears most suitable. For the flat surface, the more appropriate length scale seems to be the integral length scale $\Lambda_{zz}$, for which the thickness of the viscous sublayer is approximately equal to $\delta_v = 2\Lambda_{zz}Re^{-0.5}$, where Re is the turbulent Reynolds number (Re $= \Lambda_{zz}u'_{rms}/v$) and the thickness of the surface-influenced layer is $\sim \Lambda_{zz}$. $u'_{rms}$ is the root mean square value of the fluctuating velocity. For the test no. 64 using $H_{rms} = 0.77$ mm, the mean turbulent Reynolds number computed if the surface were flat is Re $\sim 17$ and $\delta_v \sim 0.45$ mm, whereas the surface-influenced layer should be equal to $\Lambda_{zz} \sim 1$ mm. The actual surface-influenced layer is much thicker and is approximately 2.3 mm. This result confirms the need for a different scaling whenever evident free-surface fluctuations appear. In Table 3, the comparison amongst possible length scales near the free surface is summarised for all tests.

Using the two scales that are appropriate for the present test conditions, we can define the following non-dimensional groups:

$$Fr_s = \frac{u_s}{\sqrt{gH_{rms}}}, \; Re_s = \frac{u_sH_{rms}}{v}, \; We_s = \frac{\rho u_s^2 H_{rms}}{\sigma}. \quad (15)$$

The Froude number accounts for the sharing of kinetic and gravitational energy in the free-surface fluctuations, the

**Table 3** Comparison amongst possible length scales near the free surface

| Test # | $H_{rms}$ (mm) | Re | $\delta_v$ (mm) | $\Lambda_{zz}$ (mm) | Apparent thickness (mm) |
|---|---|---|---|---|---|
| 66 | 12.09 | 1,046 | 0.25 | 4 | 36.3 |
| 65 | 10.96 | 1,033 | 0.31 | 5 | 32.9 |
| 61 | 5.25 | 792 | 0.53 | 7.5 | 15.8 |
| 62 | 2.44 | 377 | 0.52 | 5 | 7.3 |
| 63 | 1.21 | 54 | 0.35 | 1.3 | 3.6 |
| 64 | 0.77 | 17 | 0.48 | 1 | 2.3 |

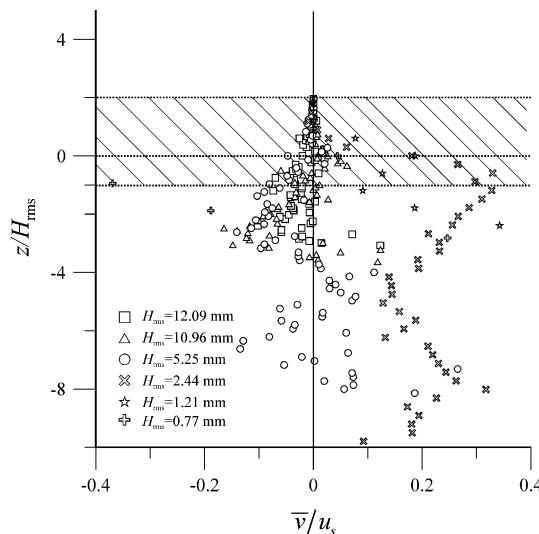**Table 4** Length, velocity scale, Froude, Reynolds and Weber numbers for the present tests

| Test # | $H_s$ (mm) | $u_s$ (mm/s) | $Fr_s$ | $Re_s$ | $We_s$ ($\times 10^{-4}$) |
|--------|------------|--------------|--------|--------|---------------------------|
| 66 | 12.09 | 130.8 | 0.38 | 1,580 | 28.4 |
| 65 | 10.96 | 103.3 | 0.32 | 1,132 | 16.1 |
| 61 | 5.25 | 52.8 | 0.23 | 277 | 2.00 |
| 62 | 2.44 | 37.7 | 0.24 | 92 | 0.48 |
| 63 | 1.21 | 20.8 | 0.19 | 25 | 0.072 |
| 64 | 0.77 | 8.6 | 0.10 | 6.6 | 0.0078 |
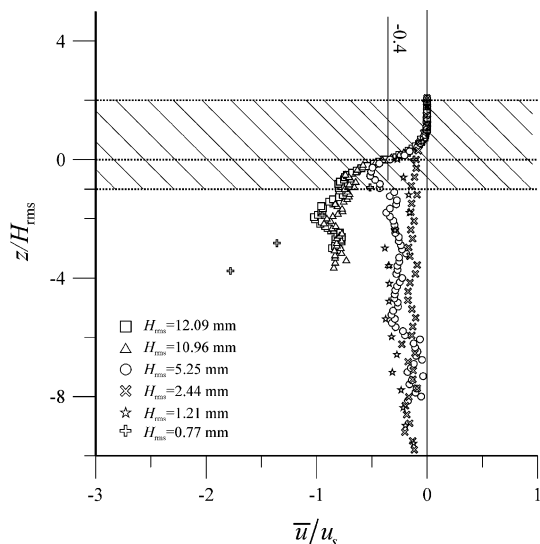


**Fig. 11** Non-dimensional streamwise mean velocity. The *dashed area* is the inner region



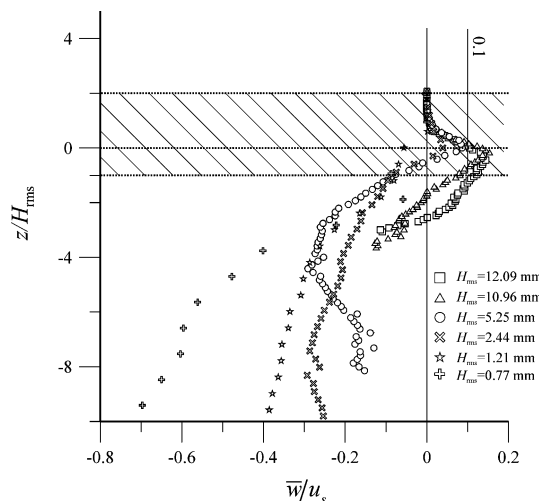**Fig. 12** Non-dimensional spanwise mean velocity. The *dashed area* is the inner region



**Fig. 13** Non-dimensional vertical mean velocity. The *dashed area* is the inner region

Reynolds number characterises the turbulent field in the free-surface boundary layer and the Weber number accounts for the relative importance of tension surface ($\sigma$ is the tension surface). The suffix s indicates that the scales used refer to the free surface.

The three numbers computed for all tests are reported in Table 4. The Froude number generally increases with $H_{rms}$, even though a plateau is observed in tests no. 61 and no. 62. The two tests have almost equal Froude numbers but $H_{rms}$ is halved, which means that under the conditions of test no. 61, part of the free-surface kinetic energy has been transformed into gravitational energy. This can be easily verified: if we assume a free-surface elevation as a monochromatic sinusoidal oscillation, this transfer of energy can be obtained as a consequence of an increase in period, whereas for a randomly distributed free-surface elevation, a transfer of this kind can be achieved with a smoothing of the fluctuations and a reduction of spikes (which accounts for a strong velocity of the free surface).

The non-dimensional velocity profiles for all tests are shown in Figs. 11, 12, and 13. As expected, the spanwise component fluctuates around zero due to the symmetry of the flow field. For the other two components, the data have much more of a tendency to collapse to a common value at the mean water level ($z = 0$), with $\overline{u} \cong -0.4u_s$ and $\overline{w} \cong 0.1u_s$, except for the two tests with the lowest Froude numbers. The mean velocity profiles collapse to a single profile after proper scaling, confirming that the set of experiments belong to a unique class of flow fields, hence a general conclusion can be drawn from their analysis.

A non-dimensional mean shear profile of the streamwise velocity is shown in Fig. 14. Most profiles have a maximum at $z = 0$ and a minimum at $z = -H_{rms}$. This is
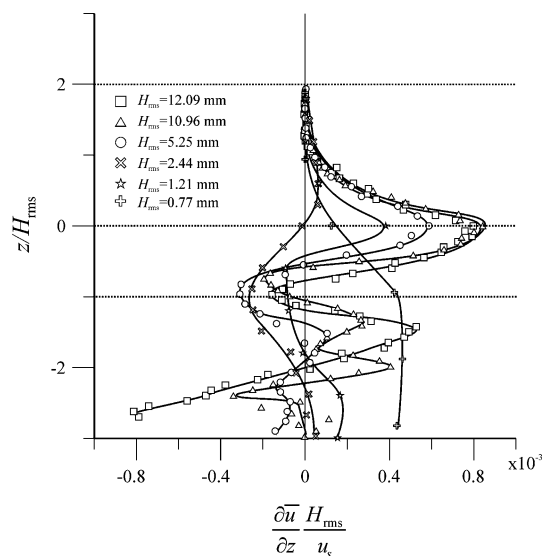
**Fig. 14** Non-dimensional mean shear profile

consistent with the results of numerical simulations by Shen et al. (2000), who suggested a detection of the boundary layer edge on the base of the position of the extrema of the mean shear profile.

## 4 Conclusions

The results show the characteristics of free-surface turbulent flows at low but non-negligible Froude numbers without the inception of air. The free-surface elevation power spectrum has a main peak at $\sim 2$ Hz, and this varies slightly with the Froude number. The height distribution in the zero(-up)-crossing analysis has a distribution quite similar to a Rayleigh distribution.

The water concentration (intermittency factor) has a quasi-normal distribution (the normal distribution is typical of a splashing regime but also of a narrow-band spectrum of free-surface waves) and has a distortion from normality in the tails.

With small Froude numbers, the free surface is almost flat and a thin boundary layer develops, with a fast damping of velocity and turbulence. With moderate Froude numbers (Fr > 0.10), a thicker boundary layer develops that has a thickness of similar magnitude to $H_{\mathrm{rms}}$. The most appropriate length and velocity scales for the description of the boundary layer are related to the free-surface statistics and are $H_{\mathrm{rms}}$ and $u_{\mathrm{s}} = \sqrt{\overline{(\mathrm{d}z_{\mathrm{s}}/\mathrm{d}t)^2}}$, respectively.

## References

Amini A (2009) Velocity profiles and interface instability in a two-phase fluid: investigations using ultrasonic velocity profiler. Exp Fluids 46:683–692

Brocchini M, Peregrine DH (2001a) The dynamics of strong turbulence at free surfaces. Part 1. Description. J Fluid Mech 449:225–254

Brocchini M, Peregrine DH (2001b) The dynamics of strong turbulence at free surfaces. Part 2. Free-surface boundary conditions. J Fluid Mech 449:255–290

Calmet I, Magnaudet J (2003) Statistical structure of high-Reynolds-number turbulence close to the free surface of an open channel flow. J Fluid Mech 474:355–378

Chanson H, Brattberg T (2000) Experimental study of the air-water shear flow in a hydraulic jump. Intl J Multiphase Flow 26(4):583–607

Dabiri D, Gharib M (2001) Simultaneous free-surface deformation and near-surface velocity measurements. Exp Fluids 30:381–390

De Cesare G, Boillat J-L (2006) Flow velocity measurements using ultrasound Doppler method—10 years experience in hydraulic modeling. In Proceedings of the 5th international symposium on ultrasonic Doppler methods for fluid mechanics and fluid engineering ISUD, pp 113–116

Dean RG (1965) Stream function representation of nonlinear ocean waves. J Geoph Res 70(18):4561–4572

Doering JC, Donelan MA (1997) Acoustic measurements of the velocity field beneath shoaling and breaking waves. Coas Eng 32(4):321–330

Eckert S, Gerbeth G (2002) Velocity measurements in liquid sodium by means of ultrasound Doppler velocimetry. Exp Fluids 32:542–546

Goda Y (2000) Random sea waves and engineering application, World Scientific Publishing

Gordon L, Oltman J (2000) Surf zone observations with a Nortek vector velocimeter and a Sontek ADV. Nortek technical note no. 014

Hong W-L, Walker DT (2000) Reynolds-averaged equations for free-surface flows with application to high-Froude number jet spreading. J Fluid Mech 417:183–209

Hurther D (2001) 3D Acoustic Doppler velocimetry and turbulence in open-channel flow. Ph.D dissertation no. 2395, Ecole polytechnique fédérale de Lausanne (EPFL), Lausanne, Switzerland

Hurther D, Lemmin U (2001) A correction method of mean turbulence measurements with a three-dimensional acoustic Doppler velocity profile. J Atmos Ocean Tech 18:446–458

Kantoush SA, De Cesare G, Boillat JL, Schleiss AJ (2008) Flow field investigation in a rectangular shallow reservoir using UVP, LSPIV and numerical modelling. Flow Meas Instr 19:139–144

Khader MHA, Elango K (1974) Turbulent pressure field beneath a hydraulic jump. J Hydraul Res 12(4):469–489

Kikura H, Yamanaka G, Aritomi M (2004) Effect of measurement volume size on turbulent flow measurement using ultrasonic Doppler method. Exp Fluids 36:187–196

Komori S, Murakami Y, Ueda H (1989) The relationship between surface-renewal and bursting motions in an open-channel flow. J Fluid Mech 203:102–123

Kraus NC, Lohrmann A, Cabrera R (1994) New acoustic meter for measuring 3D laboratory flows. J Hydr Eng 122(7):406–412

Lemmin U, Rolland T (1997) Acoustic velocity profiler for laboratory and field studies. J Hydr Eng 123(12):1089

Longo S (2006) The effects of air bubbles on ultrasound velocity measurements. Exp Fluids 41(4):593–602

Longo S, Losada IJ, Petti M, Pasotti N, Lara J (2001) Measurements of breaking waves and bores through a USD velocity profiler.

Technical report UPR/UCa_01_2001, University of Parma, University of Santander

Miles J, Ganderton P, Elliot J (2002) Vector data in the swash zone. Report. http://www.nortek-as.com/hardware/vector_swash.php

Misra SK, Kirby JT, Brocchini M, Veron F, Thomas M, Kambhamettu C (2008) The mean turbulent flow structure of a weak hydraulic jump. Phys Fluids 20, 035106, 21 pp

Nadaoka K (1986) A fundamental study on shoaling and velocity field structure of water waves in the nearshore zone. Technical report no. 36, Dept Civ Eng, Tokyo Inst Tech, 125 pp

Quiao HB, Duncan JH (2001) Gentle spilling breakers: crest flowfield evolution. J Fluid Mech 439:57–85

Reinauer R, Hager WH (1995) Non-breaking undular hydraulic jump. J Hydraul Res 33(5):683–698

Savelsberg R, Holten A, van de Water W (2006) Measurement of the gradient field of a turbulent free surface. Exp Fluids 41(4): 629–640

Settles G (2001) Schlieren and Shadowgraph techniques, visualizing phenomena in transparent media. Springer, Berlin

Shen C, Lemmin U (1997) Ultrasonic scattering in highly turbulent clear water flow. Ultras 35:57–64

Shen L, Yue DKP (2001) Large-eddy simulation of free-surface turbulence. J Fluid Mech 440:75–116

Shen L, Zhang X, Yue DKP, Triantafyllou GS (1999) The surface layer for free-surface turbulent flows. J Fluid Mech 386:167–212

Shen L, Triantafyllou GS, Yue DKP (2000) Turbulent diffusion near a free surface. J Fluid Mech 407:145–166

Takeda Y (1999a) Ultrasonic Doppler method for velocity profile measurement in fluid dynamics and fluid engineering. Exp Fluids 26:177–178

Takeda Y (1999b) Quasi periodic state and transition to turbulence in a rotating Couette system. J Fluid Mech 389:81–89

Thornton EB (1979) Energetics of breaking waves in the surf zone. J Geophys Res 84:4931–4938

Weingand A (1996) Simultaneous mapping of the velocity and deformation field at a free surface. Exp Fluids 20:358–364